INTERNATIONAL JOURNAL FOR NUMERICAL METHODS IN FLUIDS
Int. J. Numer. Meth. Fluids 2009; **59**:1369–1387
Published online 14 July 2008 in Wiley InterScience (www.interscience.wiley.com). DOI: 10.1002/fld.1874

A high-order element-based Galerkin method for the barotropic vorticity equation

Michael N. Levy[1,*,†], Ramachandran D. Nair[2] and Henry M. Tufo[3,4]

[1]*Department of Applied Mathematics, University of Colorado at Boulder, 526 UCB Boulder, CO 80309-0526, U.S.A.*
[2]*Institute for Mathematics Applied to Geosciences (IMAGe), The National Center for Atmospheric Research, PO Box 3000 Boulder, CO 80307-3000, U.S.A.*
[3]*Computational & Information Systems Laboratory (CISL), The National Center for Atmospheric Research, PO Box 3000 Boulder, CO 80307-3000, U.S.A.*
[4]*Department of Computer Science, University of Colorado at Boulder, 430 UCB Boulder, CO 80309-0430, U.S.A.*

SUMMARY

A high-order element-based Galerkin method is developed to solve the non-divergent barotropic vorticity equation (BVE). The solution process involves solving a conservative transport equation for the vorticity fields and a Poisson equation for the stream function fields. The discontinuous Galerkin method is employed for solving the transport equation and a spectral element method (continuous Galerkin) is used for the Poisson equation. A third-order strong stability preserving explicit Runge–Kutta scheme is used for time integration.

A series of tests have been performed to validate the model, which include the evolution of an idealized tropical cyclone and interaction of dual vortices in close proximity. The numerical convergence study is performed by solving the BVE on the sphere where the analytic solution is known. The test results are consistent with physical observations, and the model exhibits exponential convergence. Copyright © 2008 John Wiley & Sons, Ltd.

Received 21 December 2007; Revised 29 May 2008; Accepted 2 June 2008

KEY WORDS: barotropic vorticity equation; conservative transport; cubed sphere; discontinuous Galerkin method; Poisson problem; spectral element method

*Correspondence to: Michael N. Levy, Department of Applied Mathematics, University of Colorado at Boulder, 526 UCB Boulder, CO 80309-0526, U.S.A.
†E-mail: levym@colorado.edu

Contract/grant sponsor: DOE; contract/grant numbers: DE-FG02-04ER63870, DE-FG02-07ER64464, DE-FC03-97ER62402
Contract/grant sponsor: National Center for Atmospheric Research; contract/grant numbers: CDA-9601817, CNS-0420873, CNS-0420985, CNS-0421498
Contract/grant sponsor: NASA AIST; contract/grant number: NAG2-1646
Contract/grant sponsor: IBM Shared University Research program

1. INTRODUCTION

The barotropic vorticity equation (BVE), a simple atmospheric model, has been studied for more than half a century and is at the heart of a hierarchy of more complex models. The first successful numerical weather prediction model, by Charney *et al*. in 1950 [1], was based on the BVE. Lynch [2] provides an historical background on their work, which he describes as 'truly ground-breaking'. A barotropic atmosphere is a single-layered fluid; under this assumption there is no vertical component, and hence the equation to be solved is two dimensional (2D). For theoretical investigations of the evolution of vortices, atmospheric researchers are still using the barotropic assumption. For example, the BVE is useful for modeling the movement of tropical cyclones [3–5] and the interaction of two vortices in close proximity to one another [6]. The barotropic assumption has also been used to model global wave patterns in the middle troposphere [7, 8].

To model tropical cyclones, the computational domain is a midlatitude β-plane. The β-plane approximation is a linear approximation to the Coriolis parameter found by Taylor expansion [9]—for small displacements in latitude, scale analysis shows that the nonlinear terms are negligible. β is taken to be zero for the vortex interactions, and the global wave movement is computed on the surface of a sphere.

Most numerical models of the BVE use either finite difference or spectral method. However, local finite differences are not high-order accurate and spectral methods are global; hence, they are ill-suited for efficient parallel computing. The discontinuous Galerkin (DG) method, developed by Reed and Hill [10], is a hybrid of the finite element and finite volume methods and has been a common tool in computational sciences following the work of Cockburn and Shu [11]. DG methods are inherently conservative and high-order accurate, and they are also local; hence, they scale well across large distributed memory parallel computers. Because of these features, DG methods are widely applied in a variety of scientific and engineering problems [12, 13]. Recently, Dennis *et al*. [14] and Nair *et al*. [15] have developed a high-order DG shallow water model on a sphere. A comprehensive review of high-order element-based Galerkin method for geoscience applications is given in Levy *et al*. [16].

This paper discusses how element-based Galerkin methods can be used to model the BVE. Section 2 describes the analytic derivation of the Galerkin methods on a 2D region as well as the surface of a sphere, and Section 3 discusses the numerical results to experiments, including convergence results of the method.

2. BAROTROPIC VORTICITY EQUATION

The BVE is

$$\frac{\partial \eta}{\partial t} + \nabla \cdot [\mathbf{u}\eta] = 0 \tag{1}$$

where η is the absolute vorticity, $\nabla \cdot []$ is the divergence operator, and $\mathbf{u} = (u, v)^{\mathrm{T}}$ is a non-divergent horizontal windfield. For both the 2D and global cases, u and v are the components of the wind vector. This problem is extended to the global regime with the cubed sphere geometry, which is free from polar singularities—this is discussed in more detail in Section 2.5.

DOI: 10.1002/fld

Typically, η is decomposed to $\eta=\zeta+f$; $\zeta=\nabla\times\mathbf{u}$ is the relative vorticity (here $\nabla\times[]$ represents the 2D scalar curl); and f is the Coriolis parameter. Note that if η is evolving over time, then u and v are also changing.

To solve for $\mathbf{u}$, a stream function ψ is introduced. Since $\mathbf{u}$ is non-divergent, the Helmholtz decomposition of $\mathbf{u}$ defines ψ implicitly by

$$\mathbf{u}=\nabla^{\perp}\psi \tag{2}$$

where $\nabla^{\perp}\psi$, the 2D vector curl, is orthogonal to $\nabla\psi$ and is of equal magnitude. The direction of $\nabla^{\perp}$ is chosen such that $\nabla\times\nabla^{\perp}=\nabla^2$; hence, it follows that

$$\nabla^2\psi=\zeta \tag{3}$$

By solving the system of equations given by Equations (1) and (3), a solution to the BVE that maintains the relationship between $\mathbf{u}$ and η will be found.

2.1. 2D BVE

In two dimensions $\nabla f=(0,\beta)^{\mathrm{T}}$, where $\beta=\partial f/\partial x^2$ is the planetary vorticity gradient, a function of latitude. Equation (1) can therefore be expressed as

$$\frac{\partial\zeta}{\partial t}+\frac{\partial}{\partial x^1}[u\zeta]+\frac{\partial}{\partial x^2}[v\zeta]=-\beta v \tag{4}$$

using ζ as the prognostic variable rather than η. Typically, the planetary vorticity gradient is held constant in a β-plane approximation to some latitude [9]; hence, for this study β is a constant and the right-hand side of Equation (4) is simply a function of $\mathbf{u}$.

Equations (1) and (4) are both members of the class of conservative transport equations, which can be expressed in flux form as

$$\frac{\partial U}{\partial t}+\nabla\cdot\mathbf{F}(U)=S(U) \tag{5}$$

where U is the quantity being transported, $\mathbf{F}(U)$ is the flux function, and $S(U)$ is the source term. This is a conservative equation because, given appropriate choices of boundary conditions and $S(U)$, the integral of U over the entire domain is invariant with respect to time.

In the case of Equation (4), it is clear that $U=\zeta$, $\mathbf{F}(\zeta)=(u\zeta,v\zeta)^{\mathrm{T}}$, and $S(\zeta)=-\beta v$. For the 2D problem the computational domain, denoted by Ω, is a rectangular region with periodic boundaries in both dimensions.

2.2. Numerical procedure

To solve the BVE numerically, a spatial grid and a finite-dimensional function space are needed to represent the initial conditions. All experiments discussed herein are discretized by the discontinuous Galerkin method using rectangular elements—a Gaussian grid will be developed in one dimension and then expanded to the 2D elements via a tensor product. For the global problem, the cubed sphere geometry will map the elements onto the surface of a sphere. Tensor products of polynomials will be used as basis functions on each element.

An explicit Runge–Kutta (RK) time-stepping scheme is implemented to solve Equation (4). ψ will be found from Equation (3) and $\mathbf{u}$ will be updated from Equation (2) at each stage of the RK time step.

DOI: 10.1002/fld

2.2.1. Spatial discretization. The first step to building the numerical grid is to generate the Gauss–Legendre–Lobatto (GLL) grid on the interval $[-1,1]$. The N_g+1 node GLL grid (denoted $\{\xi_0,\ldots,\xi_{N_g}\}$) and associated quadrature weights ($\{w_0,\ldots,w_{N_g}\}$) are chosen such that

$$\int_{-1}^{1} P_n(\xi)\,\mathrm{d}\xi=\sum_{\ell=0}^{N_g} w_\ell P_n(\xi_\ell) \tag{6}$$

for all nth-degree polynomials $P_n(\xi)$ when $n<2N_g$, given the restrictions that $\xi_0=-1$ and $\xi_{N_g}=1$. The nodes are explicitly defined to be the roots of the polynomial $(1-\xi^2)L'_{N_g}(\xi)$, where $L_{N_g}(\xi)$ is the N_g-degree Legendre polynomial [17]. The weights are given by

$$w_\ell=\frac{2}{N_g(N_g+1)[L_{N_g}(\xi_\ell)]^2}$$

The N_g+1 GLL grid in one dimension is mapped to the $(N_g+1)^2$-node grid in the 2D *reference element*, $[-1,1]\times[-1,1]$ intuitively: for all ℓ,m in $\{0,\ldots,N_g\}$, (ξ_ℓ,ξ_m) is a node. The spatial domain Ω is partitioned into non-overlapping rectangular *elements* Ω^{ij}, each $\Delta x^1\times\Delta x^2$ in size, and the grid in the reference element is affinely mapped onto each element. Since -1 and 1 are part of the GLL grid, there are nodes on Γ^{ij}, the boundary of Ω^{ij} [16].

2.2.2. Function approximation. A function $f:[-1,1]\to\mathscr{R}$ can be approximated on the N_g+1 node GLL grid by polynomials of degree N_g. The easiest way to construct the polynomial approximation is by interpolating f at the node points. This can be done by constructing the Lagrange polynomials on the grid, defined by $h_\ell(\xi)$, where

$$h_\ell(\xi_m)=\begin{cases}1, & \ell=m\\ 0, & \ell\neq m\end{cases}$$

The polynomials can be expressed explicitly in the form

$$h_\ell(\xi)=\frac{(\xi-1)(\xi+1)L'_{N_g}(\xi)}{N_g(N_g+1)L_{N_g}(\xi_\ell)(\xi-\xi_\ell)}$$

and then the interpolating polynomial is given by

$$f(\xi)\approx\sum_{\ell=0}^{N_g} f_\ell h_\ell(\xi)$$

where $f_\ell=f(\xi_\ell)$. A 2D function on the reference element can be interpolated using a tensor product of the Lagrange polynomials:

$$g(\xi^1,\xi^2)\approx\sum_{\ell,m=0}^{N_g} g_{\ell m}h_\ell(\xi^1)h_m(\xi^2)$$

where $g_{\ell m}=g(\xi_\ell,\xi_m)$.

DOI: 10.1002/fld

Functions can be approximated on the entire domain Ω by piecewise approximations on each element. The functions U and ψ are approximated by U_h and ψ_h, respectively, given (for x^1, x^2 in any element Ω^{ij}) by

$$U_h(x^1, x^2, t) = \sum_{\ell,m=0}^{N_g} U_{\ell m}^{ij}(t) h_\ell(\xi^1) h_m(\xi^2)$$

$$\psi_h(x^1, x^2) = \sum_{\ell,m=0}^{N_g} \psi_{\ell m}^{ij} h_\ell(\xi^1) h_m(\xi^2)$$

Here x^1 and x^2 are affine maps from ξ^1 and ξ^2 in the reference element to the corresponding dimensions of Ω^{ij}. It should be noted that the method described in Section 2.4 to solve Equation (3) requires ψ to be continuous across element boundaries, and this condition is enforced on ψ_h, but the method in Section 2.3 for solving Equation (5) imposes no such condition on U or U_h. Despite this minor difference, both methods are high-order accurate.

2.2.3. Matrix notation. Three matrices are now introduced to simplify later derivations. The first matrix is the 1D *mass matrix*, represented by $M^{1D} = [m_{ij}]$, where $m_{ii} = w_i$ and $m_{ij} = 0$ if $i \neq j$. It should be noted that $m_{ij} \approx \int_{-1}^{1} h_i(\xi) h_j(\xi)\, d\xi$, where the integral is calculated with the GLL quadrature rule. The second matrix is the *derivative matrix*, $D = [d_{ij}]$, where $d_{ij} = h_j'(\xi_i)$, and the third matrix is $K^{1D} = [k_{ij}]$, where $k_{ij} = \int_{-1}^{1} h_i'(\xi) h_j'(\xi)\, d\xi = \sum_\ell m_{\ell\ell} d_{\ell i} d_{\ell j}$; hence, $K^{1D} = D^T M^{1D} D$ [17].

2.3. DG for advection equation

Equation (5) is rewritten in weak form by multiplying by a test function ϕ_h and integrating over each element:

$$\int_{\Omega^{ij}} \frac{\partial U_h}{\partial t} \phi_h \, dx^2 \, dx^1 + \int_{\Omega^{ij}} \nabla \cdot \mathbf{F}(U_h) \phi_h \, dx^2 \, dx^1 = \int_{\Omega^{ij}} S(U_h) \phi_h \, dx^2 \, dx^1 \tag{7}$$

ϕ_h must be in the same function space as the numerical solution U_h; hence, let

$$\phi_h(x, y) = h_p(x) h_q(y)$$

for some p, q in $\{0, \ldots, N_g\}$.

The second term in Equation (7) is integrated by parts and moved to the right-hand side of the equation, yielding

$$\int_{\Omega^{ij}} \frac{\partial U_h}{\partial t} \phi_h \, dx^2 \, dx^1 = \int_{\Omega^{ij}} S(U_h) \phi_h \, dx^2 \, dx^1 + \int_{\Omega^{ij}} (\mathbf{F}(U_h) \cdot \nabla \phi_h) \, dx^2 \, dx^1 - \int_{\Gamma^{ij}} (\mathbf{F}(U_h) \cdot \hat{\mathbf{n}}) \phi_h \, ds \tag{8}$$

where $\hat{\mathbf{n}}$ represents the normal (outward) vector to Γ^{ij}. However, continuity across element boundaries is not required for the DG method; hence, $\mathbf{F}(U_h)$ is not well defined on Γ^{ij}. It is, therefore, replaced by the numerical flux, $\hat{F}(U_h^+, U_h^-)$. The Lax–Friedrichs flux is chosen for simplicity and,

DOI: 10.1002/fld

more importantly, because it maintains the global conservation property [18]. This flux is given by the following equation:

$$\hat{F}(U_h^+, U_h^-) = \tfrac{1}{2}[(\mathbf{F}(U_h^+) + \mathbf{F}(U_h^-)) \cdot \hat{\mathbf{n}} - \bar{\alpha}(U_h^+ - U_h^-)]$$

where U_h^+ and U_h^- represent values on Γ^{ij} from the two neighboring elements and $\bar{\alpha}$ is an upper bound on the absolute value of the eigenvalues of the flux Jacobian, $\mathbf{F}'(U_h)$. Using the above numerical flux and pulling the time derivative through the spatial integral, the weak form can be expressed as

$$\frac{\partial}{\partial t}\int_{\Omega^{ij}} U_h \phi_h \, \mathrm{d}x^2 \, \mathrm{d}x^1 = \int_{\Omega^{ij}} S(U_h)\phi_h \, \mathrm{d}x^2 \, \mathrm{d}x^1 + \int_{\Omega^{ij}} (\mathbf{F}(U_h) \cdot \nabla U_h) \, \mathrm{d}x^2 \, \mathrm{d}x^1 - \int_{\Gamma^{ij}} \hat{F}(U_h^+, U_h^-)\phi_h \, \mathrm{d}s \tag{9}$$

The left-hand side of the equation is mapped from Ω^{ij} to the reference element

$$\frac{\partial}{\partial t}\int_{\Omega^{ij}} U_h \phi_h \, \mathrm{d}x^2 \, \mathrm{d}x^1 = \left(\frac{\Delta x^1 \Delta x^2}{4}\right) \times \frac{\mathrm{d}}{\mathrm{d}t}\int_{-1}^{1}\int_{-1}^{1} \sum_{\ell=0}^{N_g}\sum_{m=0}^{N_g} U_{\ell m}^{ij}(t) h_\ell(\xi^1) h_m(\xi^2) h_p(\xi^1) h_q(\xi^2) \, \mathrm{d}\xi^2 \, \mathrm{d}\xi^1$$

and the Gaussian quadrature rule from Equation (6) is used to calculate the integral term:

$$\int_{-1}^{1}\int_{-1}^{1} \sum_{\ell=0}^{N_g}\sum_{m=0}^{N_g} U_{\ell m}^{ij}(t) h_\ell(\xi^1) h_m(\xi^2) h_p(\xi^1) h_q(\xi^2) \, \mathrm{d}\xi^2 \, \mathrm{d}\xi^1 = U_{\ell m}^{ij}(t) w_\ell w_m \delta_{\ell p} \delta_{mq} = U_{pq}^{ij}(t) w_p w_q$$

Similarly, the right-hand side of Equation (9) can be calculated discretely and the equation reduces to the ordinary differential equation:

$$\frac{\partial}{\partial t} U_{pq}^{ij}(t) = \frac{4}{w_p w_q \Delta x^1 \Delta x^2}(I_{\mathbf{F}} + I_\Gamma + I_S) \tag{10}$$

where

$$I_{\mathbf{F}} = \int_{\Omega^{ij}} (\mathbf{F}(U_h) \cdot \nabla \phi_h) \, \mathrm{d}x^2 \, \mathrm{d}x^1$$

$$I_\Gamma = \int_{\Gamma^{ij}} \hat{F}(U_h^+, U_h^-)\phi_h \, \mathrm{d}s$$

$$I_S = \int_{\Omega^{ij}} S(U_h)\phi_h \, \mathrm{d}x^2 \, \mathrm{d}x^1$$

are calculated using the GLL quadrature rule [16, 19].

DOI: 10.1002/fld

Denoting the right-hand side of Equation (10) by

$$\mathscr{L}_{pq}(U)=\frac{4}{w_p w_q \Delta x^1 \Delta x^2}(I_{\mathbf{F}}+I_{\Gamma}+I_S)$$

the ordinary differential equation

$$\frac{\partial}{\partial t}U_{pq}^{ij}(t)=\mathscr{L}_{pq}(U)$$

is solved using a third-order strong stability preserving RK scheme [20]: denoting $U_{pq}^{ij}(t)$ by U^{τ} and $U_{pq}^{ij}(t+\Delta t)$ by $U^{\tau+1}$, the three-stage process for finding $U^{\tau+1}$ is

$$U^{(1)}=U^{\tau}+\Delta t\,\mathscr{L}_{pq}(U^{\tau})$$
$$U^{(2)}=\tfrac{3}{4}U^{\tau}+\tfrac{1}{4}U^{(1)}+\tfrac{1}{4}\Delta t\,\mathscr{L}_{pq}(U^{(1)})$$
$$U^{\tau+1}=\tfrac{1}{3}U^{\tau}+\tfrac{2}{3}U^{(2)}+\tfrac{2}{3}\Delta t\,\mathscr{L}_{pq}(U^{(2)})$$

Again, after each stage of the time step Equation (3) must be solved so that the windfield can be updated.

2.4. Spectral element for the Poisson equation

Unlike the advection solver, discretizing the Poisson solver on the grid discussed in Section 2.2.1 does not lead to a diagonal system—however, it does result in a sparse structure. Following the notation of Deville *et al*. the system for the 2D solver is formed using Kronecker products [17]. For the $m\times n$ matrix A and the $p\times q$ matrix B, the *Kronecker product* $A\otimes B$ is given by the $mp\times nq$ matrix:

$$A\otimes B=\begin{bmatrix} a_{11}B & a_{12}B & \dots & a_{1q}B \\ a_{21}B & a_{22}B & \dots & a_{2q}B \\ \vdots & \vdots & \ddots & \vdots \\ a_{p1}B & a_{p2}B & \dots & a_{pq}B \end{bmatrix}$$

As with Equation (5), the first step in solving Equation (3) is to rewrite it in weak form. The spectral element method requires continuity across element boundaries, so the weak form is an integral over the entire domain:

$$\sum_{i,j}\int_{\Omega^{ij}}(\nabla^2\psi_h)\phi_h\,\mathrm{d}x^2\,\mathrm{d}x^1=\sum_{i,j}\int_{\Omega^{ij}}\zeta_h\phi_h\,\mathrm{d}x^2\,\mathrm{d}x^1$$

Representing ψ_h and ζ_h as in Section 2.2.2 and integrating the left-hand side by parts, the weak form can be rewritten as

$$-\sum_{i,j,\ell,m}\psi_{\ell m}^{ij}\int_{\Omega^{ij}}(h'_{\ell}(\xi^1)h'_p(\xi^1)h_m(\xi^2)h_q(\xi^2)+h_{\ell}(\xi^1)h_p(\xi^1)h'_m(\xi^2)h'_q(\xi^2))\,\mathrm{d}x^2\,\mathrm{d}x^1$$
$$=\sum_{i,j,\ell,m}\zeta_{\ell m}^{ij}\int_{\Omega^{ij}}h'_{\ell}(\xi^1)h'_p(\xi^1)h_m(\xi^2)h_q(\xi^2)\,\mathrm{d}x^2\,\mathrm{d}x^1 \tag{11}$$

DOI: 10.1002/fld

Using the matrix notation from Section 2.2.3, define the matrices K^{ij} and M^{ij} by

$$K^{ij} = -\left(\frac{\Delta x^2}{\Delta x^1}(K^{1D} \otimes M^{1D}) + \frac{\Delta x^1}{\Delta x^2}(M^{1D} \otimes K^{1D})\right)$$

$$M^{ij} = \frac{\Delta x^1 \Delta x^2}{4}(M^{1D} \otimes M^{1D})$$

The integrals in Equation (11) can then be expressed as a matrix multiply:

$$K^{ij}\boldsymbol{\psi} = M^{ij}\boldsymbol{\zeta} \tag{12}$$

where $\boldsymbol{\psi}$ and $\boldsymbol{\zeta}$ are vectors representing $\psi^{ij}_{\ell m}$ and $\zeta^{ij}_{\ell m}$ using natural ordering. Equation (12) holds on individual elements Ω^{ij}, and the global matrices K and M are constructed via the process of global assembly or direct stiffness summation, as described in [21]:

$$K = \bigwedge_{ij} K^{ij} \quad \text{and} \quad M = \bigwedge_{ij} M^{ij}$$

The partial differential equation in (3) has been reduced to the linear system $K\psi = M\zeta$. Since K is symmetric, real, and positive definite, the system can be solved using the conjugate gradient method (a direct solve is impractical, due to the size and structure of K). Once ψ is found, u and v can be updated by

$$u = -\frac{\partial \psi}{\partial x^2} = -\frac{2}{\Delta x^2}(D \otimes I)\boldsymbol{\psi} \quad \text{on } \Omega^{ij}$$

$$v = \frac{\partial \psi}{\partial x^1} = \frac{2}{\Delta x^1}(I \otimes D)\boldsymbol{\psi} \quad \text{on } \Omega^{ij}$$

where I represents the $(N_g+1)\times(N_g+1)$ identity matrix.

2.5. Global BVE

Equation (1) is also a member of the class of conservative transport equations, with $U = \eta$, $\mathbf{F}(\eta) = \mathbf{u}\eta$, and $S(\eta) = 0$. Again, it is important to note that $\mathbf{u}$ is evolving over time, since the non-divergent wind and vorticity are related by

$$\nabla^2 \psi = \eta - f \tag{13}$$

and Equation (2) still defines the relationship between $\mathbf{u}$ and ψ.

Typically, position and the velocity vector are defined on the surface of a sphere as functions of latitude and longitude (θ and λ). Because of the polar singularities associated with the lat-long geometry, using an element-based Galerkin method in this geometry is not efficient. The cubed sphere geometry avoids the pole problem by inscribing the sphere with a cube and using a central (gnomonic) projection from the sphere to the cube [22, 23]. Each face of the cubed sphere can then be partitioned into elements.

2.5.1. Cubed sphere geometry. The faces of the cube are labeled from 1 to 6 such that the intersection of the equator and the prime meridian is projected to the center of face 1, the equator bisects faces 1 through 4, the north pole is projected to the center of face 5, and the south pole to

DOI: 10.1002/fld

the center of face 6. Each face has a local Cartesian coordinate system, (x, y), with $x, y \in [-a, a]$ where $a = R/\sqrt{3}$ and R is the radius of the sphere. Previous research has shown that superior results are obtained using an equi-spaced element grid on the (x^1, x^2) coordinate system [19], where $x = a\tan x^1$, $y = a\tan(x^2)$, and $x^1, x^2 \in [-\pi/4, \pi/4]$.

Define $\mathbf{a}_1$ and $\mathbf{a}_2$ as the covariant base vectors $\partial\mathbf{r}/\partial x^1$ and $\partial\mathbf{r}/\partial x^2$, respectively, where $\mathrm{d}\mathbf{r} = R\cos\theta\,\mathrm{d}\lambda\hat{\mathbf{e}}_\lambda + R\,\mathrm{d}\theta\hat{\mathbf{e}}_\theta$ is a small displacement on the surface, $\hat{\mathbf{e}}_\lambda$ is the unit vector in the east–west direction, and $\hat{\mathbf{e}}_\theta$ is the unit vector in the north–south direction. The covariant components of $\mathbf{u}$ are given by $u_1 = \mathbf{v}\cdot\mathbf{a}_1$ and $u_2 = \mathbf{v}\cdot\mathbf{a}_2$, and the contravariant components u^1 and u^2 are expressed as $\mathbf{u} = u^1\mathbf{a}_1 + u^2\mathbf{a}_2$.

A is the transformation matrix between the cube and the sphere, given by

$$A = R\begin{bmatrix} \cos\theta\partial\lambda/\partial x^1 & \cos\theta\partial\lambda/\partial x^2 \\ \partial\theta/\partial x^1 & \partial\theta/\partial x^2 \end{bmatrix} = [\mathbf{a}_1 \;\; \mathbf{a}_2]$$

The metric tensor of the transformation is defined as $g_{ij} = \mathbf{a}_i\cdot\mathbf{a}_j = A^{\mathrm{T}}A$. Covariant and contravariant components are related via g_{ij} by the relationships $u_i = g_{ij}u^j$ and $u^i = g^{ij}u^j$, where $g^{ij} = (g_{ij})^{-1}$.

On all six faces of the cube,

$$g_{ij} = \frac{R^2}{\rho^4\cos^2 x^1\cos^2 x^2}\begin{bmatrix} 1+\tan^2 x^1 & -\tan x^1\tan x^2 \\ -\tan x^1\tan x^2 & 1+\tan^2 x^2 \end{bmatrix} \tag{14}$$

where $\rho = (1+\tan^2 x^1+\tan^2 x^2)^{1/2}$. Let $g = \det(g_{ij})$; hence $\sqrt{g} = R^2/(\rho^3\cos^2 x^1\cos^2 x^2)$. The transformations between the spherical velocity components and the cubed sphere components are [19]

$$A^{\mathrm{T}}\begin{bmatrix} u \\ v \end{bmatrix} = \begin{bmatrix} u_1 \\ u_2 \end{bmatrix} \quad \text{and} \quad A^{-1}\begin{bmatrix} u \\ v \end{bmatrix} = \begin{bmatrix} u^1 \\ u^2 \end{bmatrix}$$

Note that the transformation matrix A and the resulting metric term $\sqrt{g}$ are free of singularities, even at the poles.

2.5.2. Integration and differentiation on the cubed sphere. The gradient, divergence, and curl operators are defined in terms of $\nabla_g = (\partial/\partial x^1, \partial/\partial x^2)^{\mathrm{T}}$ on a face of the cubed sphere as follows [23]:

$$\nabla f = A^{-\mathrm{T}}\nabla_g f$$

$$\nabla\cdot\mathbf{f} = \frac{1}{\sqrt{g}}\nabla_g\cdot[\sqrt{g}A^{-1}\mathbf{f}]$$

$$\nabla\times\mathbf{f} = \frac{1}{\sqrt{g}}\nabla_g\times[A^{\mathrm{T}}\mathbf{f}]$$

Rectangular elements are arranged on the sphere, as in Figure 1. To integrate over the entire sphere, integrals over each element on the cubed sphere are summed:

$$\int_{-\pi/2}^{\pi/2}\int_0^{2\pi} f(\lambda,\theta)R^2\cos\theta\,\mathrm{d}\lambda\,\mathrm{d}\theta = \sum_{i,j}\int_{\Omega^{ij}} f(x^1, x^2)\,\mathrm{d}\Omega \tag{15}$$

DOI: 10.1002/fld

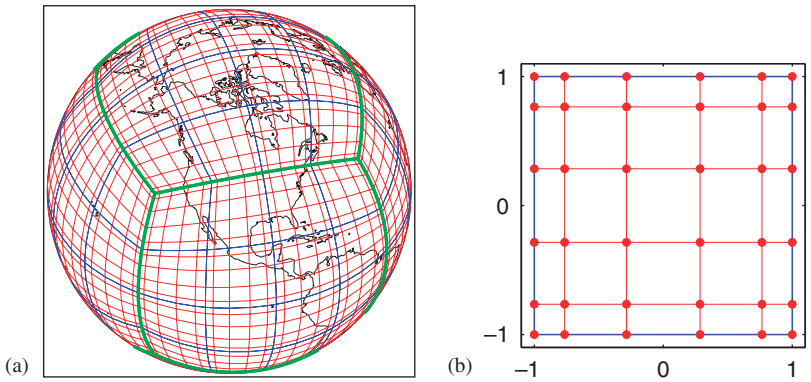

Figure 1. (a) Earth tiled with 96 elements (thin solid lines), each with a 6-node GLL grid (dotted lines). Thick solid lines outline the cube faces. (b) 6×6 GLL grid on the reference element.

where $\mathrm{d}\Omega=\sqrt{g}\,\mathrm{d}x^2\,\mathrm{d}x^1$. As mentioned in the previous section, $\sqrt{g}$ is the metric term associated with the mapping from the surface of the sphere to the cubed sphere [19].

2.5.3. Solving the transport equation on a cubed sphere. In curvilinear coordinates, using the properties described in the previous section, Equation (1) takes the form

$$\frac{\partial\eta}{\partial t}+\frac{1}{\sqrt{g}}\nabla_g\cdot[\sqrt{g}A^{-1}\mathbf{u}\eta]=0$$

hence the weak form is

$$\int_{\Omega^{ij}}\frac{\partial\eta}{\partial t}\phi_h\,\mathrm{d}\Omega+\int_{\Omega^{ij}}\frac{1}{\sqrt{g}}\nabla_g\cdot[\sqrt{g}A^{-1}\mathbf{u}\eta]\phi_h\,\mathrm{d}\Omega=0$$

Noting that $A^{-1}\mathbf{u}$ is the contravariant windfield, $\mathrm{d}\Omega=\sqrt{g}\,\mathrm{d}x^2\,\mathrm{d}x^1$, and $\sqrt{g}$ has no time dependence, the weak form simplifies to

$$\int_{\Omega^{ij}}\frac{\partial}{\partial t}[\sqrt{g}\eta]\,\mathrm{d}x^2\,\mathrm{d}x^1+\int_{\Omega^{ij}}\frac{\partial}{\partial x^1}[u^1\sqrt{g}\eta]\,\mathrm{d}x^2\,\mathrm{d}x^1+\int_{\Omega^{ij}}\frac{\partial}{\partial x^2}[u^2\sqrt{g}\eta]\,\mathrm{d}x^2\,\mathrm{d}x^1=0 \tag{16}$$

Note that Equation (16) is of the same form as Equation (7), with prognostic variable $U=\sqrt{g}\eta$, flux function $\mathbf{F}(\sqrt{g}\eta)=(u^1\sqrt{g}\eta,u^2\sqrt{g}\eta)^{\mathrm{T}}$, and source term $S(\sqrt{g}\eta)=0$. Thus, $\int_\Omega\eta\sqrt{g}\,\mathrm{d}x^2\,\mathrm{d}x^1$ will be invariant; hence, η is conserved on the global scale.

The only computational difference between the 2D implementation and the cubed sphere implementation is in the flux calculations along the edges of the cube (the calculations are identical on each face). In the 2D algorithm, all the elements used the same coordinate system; a local coordinate system is used on each face of the cubed sphere. For the flux calculations, velocity vectors along the boundary between two faces need to be mapped to spherical (lat-long) coordinates and then mapped back onto the neighboring face.

DOI: 10.1002/fld

2.5.4. Solving the Poisson equation on a cubed sphere. Following from Section 2.5.2, the Laplacian can also be derived on the cubed sphere in the local coordinate system:

$$\begin{aligned}\nabla^2\psi &= \nabla\cdot\nabla\psi \\ &= \frac{1}{\sqrt{g}}\nabla_g\cdot[\sqrt{g}A^{-1}A^{-\mathrm{T}}\nabla_g\psi]\end{aligned}$$

The weak form of Equation (3) on element Ω^{ij} is

$$\sum_{i,j}\int_{\Omega^{ij}}\nabla_g\cdot[\sqrt{g}A^{-1}A^{-\mathrm{T}}\nabla_g\psi]\phi_h\,\mathrm{d}x^2\,\mathrm{d}x^1=\sum_{i,j}\int_{\Omega^{ij}}\sqrt{g}(\eta-f)\phi_h\,\mathrm{d}x^2\,\mathrm{d}x^1$$

or, integrating by parts and rearranging terms,

$$-\sum_{i,j}\int_{\Omega^{ij}}[A^{-\mathrm{T}}\nabla_g\psi]\cdot[A^{-\mathrm{T}}\nabla_g\phi_h]\sqrt{g}\,\mathrm{d}x^2\,\mathrm{d}x^1=\sum_{i,j}\int_{\Omega^{ij}}(\eta-f)\phi_h\sqrt{g}\,\mathrm{d}x^2\,\mathrm{d}x^1$$

This can again be reduced to the form of Equation (12)

$$\bigwedge_{ij}K^{ij}\boldsymbol{\psi}=\bigwedge_{ij}M^{ij}(\boldsymbol{\eta}-\mathbf{f})$$

but K^{ij} and M^{ij} vary from element to element (increasing the memory usage of the algorithm).

2.6. Filtering high-order modes

The nonlinear flux term in the BVE can cause instabilities; hence, some filters were considered. For the 2D experiments, tests were conducted with a numerical diffusion term ($\varepsilon\nabla^2\zeta$, where $0<\varepsilon\ll 1$) on the right-hand side of Equation (4). Visually there was no significant benefit in the numerical results, though; hence, the diffusion term was omitted in the results presented in Section 3.1.

To reduce high-order noise, a Boyd–Vandeven filter [24] was used. The filter was chosen based on a previous study of an element-based Galerkin solver for the shallow water equations [25], and parameters for the filter were also chosen based on that work. The Boyd–Vandeven filter of order p, applied on the 1D reference element, has the form

$$\sigma(\xi)=\frac{1}{2}\mathrm{erfc}\left(2\sqrt{p}\left(|\xi|-\frac{1}{2}\right)\sqrt{\frac{-\log(1-4(|\xi|-\frac{1}{2})^2}{4(|\xi|-\frac{1}{2})^2}}\right)$$

where erfc is the complimentary error function, defined by

$$\mathrm{erfc}(x)=\frac{2}{\sqrt{\pi}}\int_x^\infty \mathrm{e}^{-r^2}\,\mathrm{d}r$$

To apply the filter, recall that functions on our reference element are approximated polynomials of degree N_g. Although this study uses the Lagrange basis functions described in Section 2.2.2, the function $f(\xi)$ can also be approximated using Legendre basis functions:

$$f(\xi)\approx\sum_{\ell=0}^{N_g}\hat{f}_\ell L_\ell(\xi),\quad \hat{f}_\ell=\frac{2\ell+1}{2}\int_{-1}^{1}f(\xi)L_\ell(\xi)\,\mathrm{d}\xi$$

DOI: 10.1002/fld

The filtered function, $\tilde{f}(\xi)$, is given by

$$\tilde{f}(\xi)=(1-\mu)f(\xi)+\mu\sum_{\ell=0}^{N_g} w_\ell \hat{f}_\ell L_\ell(\xi)$$

where the weights w_ℓ are given by

$$w_\ell=\begin{cases}1, & \ell<s\\ \sigma\left(\dfrac{\ell-s}{N_g-s}\right), & s\leqslant\ell\leqslant N_g\end{cases}$$

Following from the results of Taylor *et al*., the filter was applied every 20 min of model time using parameters $p=12$, $\mu=0.2$, and $s=2N_g/3$ for the results discussed in Section 3.2.

3. NUMERICAL EXPERIMENTS

Two 2D experiments are discussed in this section. Neither have analytic solutions, but both are based around physical phenomenon; hence, the expected behavior is known. The first test, taken from DeMaria [4], arises from the fact that tropical cyclones drift to the northwest in the northern hemisphere (for simplicity, all discussion will assume a counter-clockwise vortex in the northern hemisphere), and the second, taken from Shin *et al*. [6], is based on two same-sign vortices rotating around each other; depending on the distance separating the two, they will either merge into one vortex or repel each other.

A global experiment is discussed as well—unlike the 2D cases, it has a known analytic solution. The test is the propagation of a global wave, taken from Gates and Riegel [7]. Because the true solution is known, convergence results are also presented.

3.1. 2D experiments

The BVE assumes a non-divergent wind; hence, the initial wind profile for a vortex centered at (x_0, y_0) can be expressed in terms of the tangential wind $V(r)$ (where $r=\sqrt{(x-x_0)^2+(y-y_0)^2}$ is the distance from the point (x, y) in the plane to the center of the vortex). Since $V(r)$ is the tangential wind, it follows that

$$u(x, y)=-V(r)(y-y_0)/r \tag{17}$$

$$v(x, y)=V(r)(x-x_0)/r \tag{18}$$

with $u(x_0, y_0)$ and $v(x_0, y_0)$ both defined to be 0. Since $\zeta=\nabla\times\mathbf{u}$, the initial vorticity is

$$\zeta(r)=\begin{cases}V'(r)+V(r)/r, & r\neq 0\\ 2V'(0), & r=0\end{cases} \tag{19}$$

3.1.1. Drifting topical cyclone. Specifically, the first test uses an initial tangential wind given by

$$V(r)=\frac{2V_m r\exp[-a(r/r_m)^b]}{r_m[1+(r/r_m)^2]} \tag{20}$$

DOI: 10.1002/fld

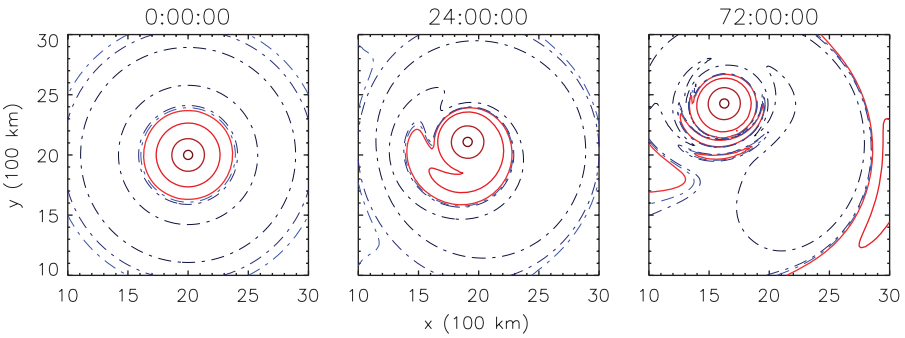

Figure 2. Contours of the vorticity field in the tropical cyclone test case, shown after 24 and 72 h. Solid contours are positive and dash-dot contours are negative. Calculations were done on a 100 by 100 grid of elements using cubic interpolants (4 by 4 GLL grid).

yielding an initial vorticity

$$\zeta(r) = 2V_m(2 - ab[(r/rm)^b + (r/rm)^{b+2}])\frac{\exp[-a(r/r_m)^b]}{1+(r/r_m)^2}$$

Here $V_m = 30\,\text{m/s}$, $r_m = 80\,\text{km}$, $a = 10^{-6}$, and $b = 6$. The domain is a 4000 km by 4000 km square and periodic, and β is calculated at the latitude 20°N.

The initial vortex was centered at (2000 km, 2000 km) [4]. The computational grid was 100×100 elements, each overlaid with a 4×4 GLL grid. As seen in Figure 2, the vortex drifted to the northwest as expected. For clarity, the figure only displays the center of the computational domain.

The element-based Galerkin results are similar to the results in [4]; after 24 h the cyclone is drifting to the northwest at a roughly constant velocity. One difference between the spectral method in the original study and the EBG method is resolution—more gridpoints were used in this study to allow for better visualization of the cyclone.

3.1.2. Interactions between vortices. The second test uses an initial vorticity profile based on two vortices with tangential wind given by

$$V(r) = \frac{V_m r}{r_m}\exp\{[1-(r/r_m)^b]/b\} \tag{21}$$

Following from Equation (19), the initial vorticity is

$$\zeta(r) = \frac{V_m[2-(r/r_m)^b]}{r_m}\exp\{[1-(r/r_m)^b]/b\}$$

the same form found in [3, 26]. In this case, $V_m = 30\,\text{m/s}$, $r_m = 120\,\text{km}$, and b is calculated so that $V(r) = 15\,\text{m/s}$ when $r = 300\,\text{km}$ (hence, $b \approx 1.132$). The distance between the center of the two vortices is parameterized by d, the domain is a 12000 km by 12000 km periodic square, and β is taken to be 0.

This test was broken into two portions—two vortices that converged ($d = 400\,\text{km}$), and two that diverged ($d = 600\,\text{km}$). Both portions were calculated on the same domain, with a 100×100 mesh of elements overlaid by a 4×4 GLL grid. The vortices in the convergent case, seen in Figure 3,

DOI: 10.1002/fld

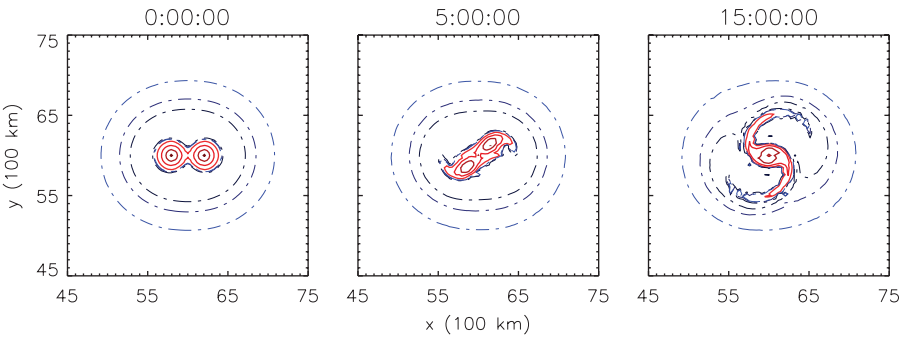

Figure 3. Contours of the vorticity field of 2 vortices merging, shown after 5 and 15 h. Solid contours are positive, dash-dot contours are negative. Calculations were done on a 100 by 100 grid of elements using cubic interpolants (4 by 4 GLL grid).

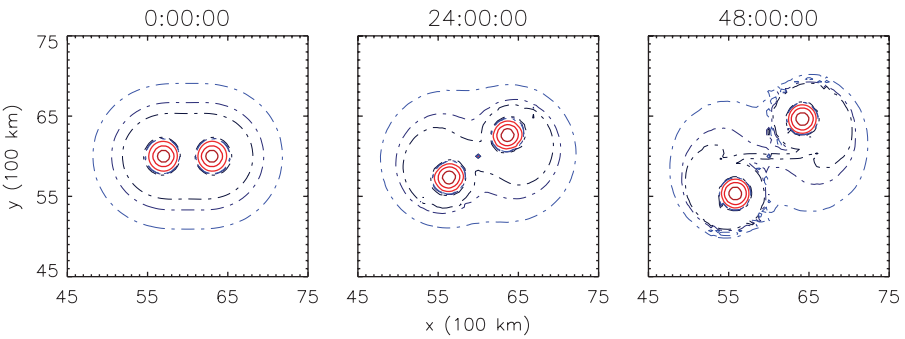

Figure 4. Contours of the vorticity field of 2 vortices repelling, shown after 24 and 48 h. Solid contours are positive, dash-dot contours are negative. Calculations were done on a 100 by 100 grid of elements using cubic interpolants (4 by 4 GLL grid).

were centered at (5800 km, 6000 km) and (6200 km, 6000 km), whereas the divergent vortices, seen in Figure 4, were centered at (5700 km, 6000 km) and (6300 km, 6000 km). Again, only a portion of the domain is displayed in the figures.

The results in this section are very similar to the test results by Shin *et al.* [6]—the velocity and path predicted were indistinguishable between the two methods. Both tests used similar resolutions; Shin *et al.* used a fourth-order finite difference scheme with 300 equally spaced nodes, and the EBG method discussed here also had 300 nodes, albeit not equally spaced.

3.2. Global wave propagation

A solution to the global BVE is described by the following stream function [7, 27]:

$$\psi = A\sin(m\lambda - vt)L_n^m(\sin(\theta)) - BR^2\sin\theta + CL_n(\sin\theta) \tag{22}$$

Although ψ is typically not the variable of interest, recall that $\eta = \nabla^2\psi + f$ and $\mathbf{u} = \nabla^\perp\psi$.

DOI: 10.1002/fld

In Equation (22), A, B, and C are arbitrary constants, m is the hemispheric wave number, and v/m is the phase speed of the wave. As in Section 2.2.1, L_n is the n-degree Legendre polynomial, and L_n^m is an associated Legendre function. For this particular test, the following parameters were used:

$$m=6$$

$$n=7$$

$$v/m=20^\circ\text{longitude/day}$$

$$A=1000\,\text{m}^2/\text{s}$$

$$B=\frac{n(n+1)}{n(n+1)-2}\left(\frac{v}{m}+\frac{2\Omega}{n(n+1)}\right)\approx 6.89\times 10^{-6}\,\text{s}^{-1}$$

$$C=0$$

Thus, the full solution set is given by

$$\eta(\lambda,\theta,t)=2\sin\theta\left(B-\frac{28\tilde{A}\cos^6\theta\sin(6\lambda-vt)}{R^2}\right)+2\Omega\sin\theta$$

$$\psi(\lambda,\theta,t)=\frac{\sin\theta}{R^2}(\tilde{A}\cos^6\theta\sin\theta\sin(6\lambda-vt)-BR^2)$$

$$u(\lambda,\theta,t)=RB\cos\theta-\frac{\tilde{A}\cos^5\theta(7\cos(2\theta)-5)\sin(6\lambda-vt)}{2R}$$

$$v(\lambda,\theta,t)=\frac{6\tilde{A}\cos^5\theta\cos(6\lambda-vt)\sin\theta}{R}$$

where $\tilde{A}=135\,135A$ (chosen because $L_7^6(\sin\theta)=135\,135\cos^6\theta\sin\theta$). The initial conditions found by taking $t=0$ and, as with the steady state test case, the simulation was run for 5 days. The numerical solution is compared with the analytic solution in Figure 5.

3.2.1. Accuracy of the method. Since this experiment has a known analytic solution, the error between the true solution and the numerical solution can be found. The relative L_2-error between the numerical solution $U_h(\lambda,\theta)$ and the true solution $U(\lambda,\theta)$ is used to measure the accuracy of the numerical method. The error is given by the formula

$$\varepsilon=\left[\frac{\int_\Omega[U_h(\lambda,\theta)-U(\lambda,\theta)]^2\,\text{d}\Omega}{\int_\Omega[U(\lambda,\theta)]^2\,\text{d}\Omega}\right]^{1/2}$$

and the integrals are calculated using the GLL quadrature on each element on the cubed sphere. The way the domain is partitioned, the number of nodes can be increased by either using a finer GLL grid (increasing N_g) or using more elements to cover the domain (increasing N_e). The former is the p-error and the latter is the h-error. Figures 6 and 7 show the error in η, ψ, and $\mathbf{u}$.

Figure 6 plots the p-error using 150 elements to tile the cubed sphere (a 5 by 5 mesh of elements on each face). Figure 6(a) shows the error without any filtering, and Figure 6(b) shows the error

DOI: 10.1002/fld

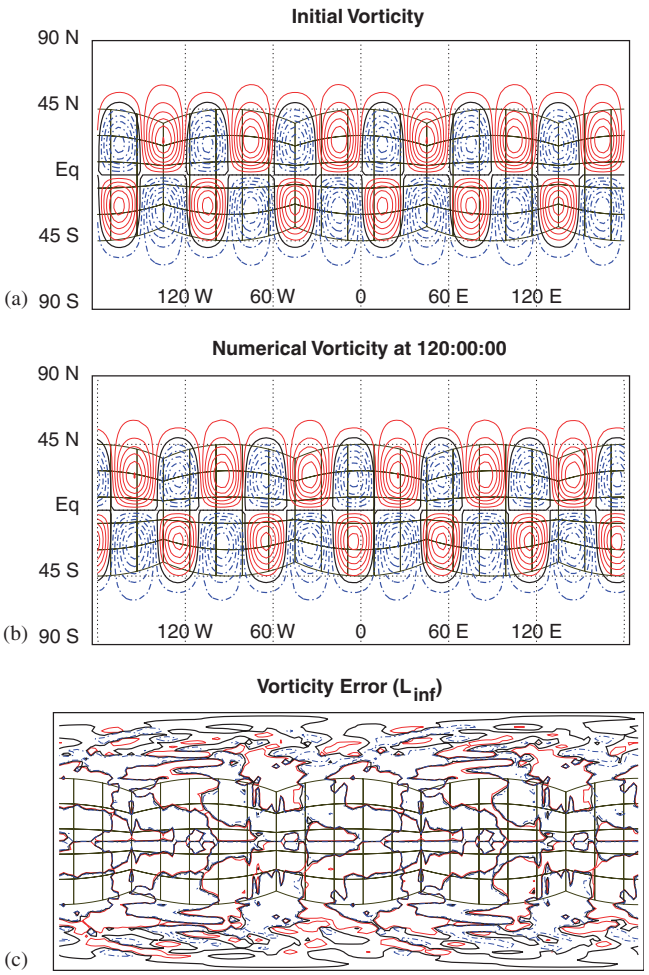

Figure 5. (a) The initial field for η; (b) the numerical solution for η after 5 (simulated) days with $N_e = 150$ and $N_g = 5$; (c) the error between the numerical and analytic solution for η. The contour interval for (a) and (b) is $7 \times 10^{-6}\,\mathrm{s}^{-1}$, while for (c) it is $5 \times 10^{-9}\,\mathrm{s}^{-1}$. Again solid contours are positive values while dash-dot contours are negative. Elements on the equatorial faces of the cubed sphere are also shown. Note that the wave has a horizontal velocity of 20° per day, moving from west to east; hence, the wave has shifted east 100° from plot (a) to (b).

with the BV filter from Section 2.6. The filtering improves the solution of the stream function, especially as N_g grows, but does not have a drastic effect on the convergence rate of the wind field or the absolute vorticity (the error in those two variables decreases roughly by a factor of 10 when the order of each element is increased by one, regardless of filtering).

Figure 7 plots the h-error using 6th-order elements to tile the cubed sphere (a 6 by 6 GLL grid on each element). Figure 7(a) shows the error without any filtering, and Figure 7(b) shows the error with the BV filter from Section 2.6. The filtering improves the solution by about an order of

DOI: 10.1002/fld

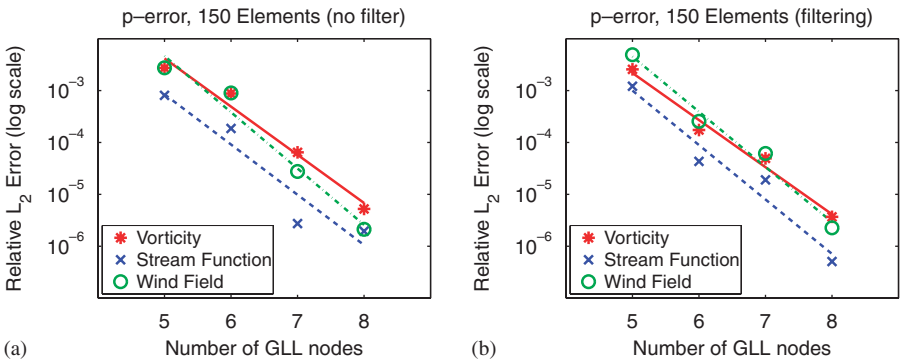

Figure 6. p-Error plot for the global experiment with $N_e = 150$: (a) without filtering and (b) with filtering. The lines drawn are the least-squares fit.

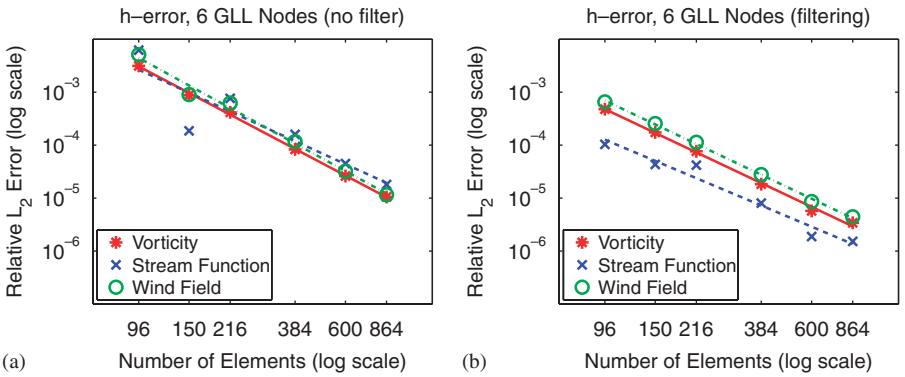

Figure 7. h-Error plot for the global experiment with $N_g = 5$: (a) without filtering and (b) with filtering. The lines drawn are the least-squares fit.

accuracy, but again does not affect the convergence rate (the error in all three variables decreases roughly by a factor of five when the number of elements is doubled, regardless of filtering).

3.2.2. Conservation of absolute vorticity and enstrophy. Conservation of integral invariants can be monitored with the normalized integral

$$\bar{U}_h(t) = \frac{\int_{-\pi/2}^{\pi/2} \int_0^{2\pi} (U_h(\lambda, \theta, t) - U_h(\lambda, \theta, 0)) R^2 \cos\theta \, \mathrm{d}\lambda \, \mathrm{d}\theta}{\int_{-\pi/2}^{\pi/2} \int_0^{2\pi} U_h(\lambda, \theta, 0) R^2 \cos\theta \, \mathrm{d}\lambda \, \mathrm{d}\theta}$$

calculated with the GLL quadrature rule on the cubed sphere. The conservation of η^2 is measured in this manner, and the time trace is shown in Figure 8(b). Although the normalized integral decreases slightly, it is consistent with other numerical results using conservative methods [28].

DOI: 10.1002/fld

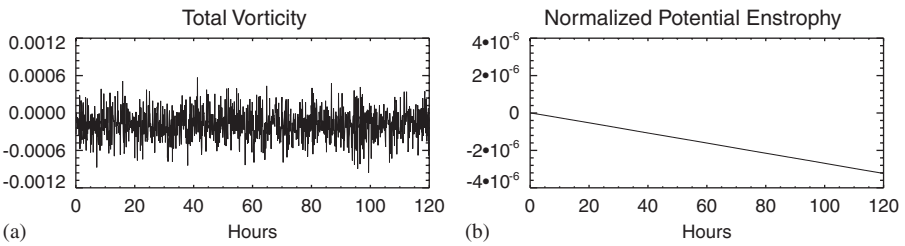

Figure 8. Time traces of (a) total absolute vorticity and (b) normalized potential enstrophy with 150 elements and a 6×6 GLL grid on each element (with BV filtering).

This metric is not used to show the conservation of η because, for the test case described in Section 3.2,

$$\int_{-\pi/2}^{\pi/2} \int_{0}^{2\pi} \eta(\lambda, \theta, t) R^2 \cos\theta \, \mathrm{d}\lambda \, \mathrm{d}\theta \equiv 0$$

Clearly the denominator of the normalized integral would be zero; hence, Figure 8(a) shows the total absolute vorticity, given by

$$\int_{-\pi/2}^{\pi/2} \int_{0}^{2\pi} \eta(\lambda, \theta, t) R^2 \cos\theta \, \mathrm{d}\lambda \, \mathrm{d}\theta$$

As the figure shows, the total vorticity oscillates around 0.

4. CONCLUSION

This paper discussed the feasibility of a high-order element-based Galerkin method for solving the BVE. The BVE was cast in flux form and solved using a DG method with an explicit RK time integration. At each stage of the RK integration, the windfield was updated by solving a Poisson problem for the stream function.

Two tests showed the results of the Galerkin method were consistent with known physical behavior. Specifically, a tropical cyclone drifted to the northwest, and two vortices in close proximity interacted as expected. A third test, with an analytic solution [27], showed the method converges exponentially.

The method is already being extended to model the nonlinear shallow water equations, cast in vorticity–divergence form. Future work also includes a scalability study—the transport solver has been parallelized efficiently, but more work is needed to improve the Poisson solver.

ACKNOWLEDGEMENTS

Support for this work was provided by DOE Grants #DE-FG02-04ER63870, #DE-FG02-07ER64464, and DE-FC03-97ER62402, as well as NSF sponsorship of the National Center for Atmospheric Research. Computer time was provided by NSF ARI Grant #CDA-9601817, NSF MRI Grant #CNS-0420873, NSF MRI Grant #CNS-0420985, NSF MRI Grant #CNS-0421498, NASA AIST Grant #NAG2-1646, and a grant from the IBM Shared University Research (SUR) program. Additionally, the authors would like to thank two anonymous reviewers for their comments and suggestions.

DOI: 10.1002/fld

REFERENCES

1. Charney JG, Fjörtoft R, von Neumann JG. Numerical integration of the barotropic vorticity equation. *Tellus* 1950; **2**(4):237–254.
2. Lynch P. The origins of computer weather prediction and climate modeling. *Journal of Computational Physics* 2008; **227**(7):3431–3444.
3. Chan JCL, Williams RT. Analytical and numerical studies of the beta-effect in tropical cyclone motion. Part I: zero mean flow. *Journal of the Atmospheric Sciences* 1987; **44**(9):1257–1265.
4. DeMaria M. Tropical cyclone motion in a nondivergent barotropic model. *Monthly Weather Review* 1985; **113**(7):1199–1210.
5. Rossby CG. On displacements and intensity changes of atmospheric vortices. *Journal of Marine Research* 1948; **7**:175–187.
6. Shin SE, Han JY, Baik JJ. On the critical separation distance of binary vortices in a nondivergent barotropic atmosphere. *Journal of the Meteorological Society of Japan* 2006; **84**(5):853–869.
7. Gates WL, Riegel CA. A study of numerical errors in the integration of barotropic flow on a spherical grid. *Journal of Geophysical Research* 1962; **67**(2):773–784.
8. Williamson DL. Integration of the barotropic vorticity equation on a spherical geodesic grid. *Tellus* 1968; **20**(4):642–653.
9. Holton JR. *An Introduction to Dynamic Meteorology* (4th edn). Elsevier Academic Press: Burlington, MA, 2004.
10. Reed WH, Hill TR. Triangular mesh methods for the neutron transport equation. *Los Alamos Scientific Laboratory Report LA-UR-73-479*, 1973.
11. Cockburn B, Shu CW. TVB Runge–Kutta local projection discontinuous Galerkin finite element method for conservation laws II: general framework. *Mathematics of Computation* 1989; **52**(186):411–435.
12. Cockburn B, Karniadakis GE, Shu C-W. *Discontinuous Galerkin Methods*: *Theory*, *Computation*, *and Applications.* Springer: Berlin, Germany, 2000.
13. Remacle J-F, Flaherty JE, Shephard MS. An adaptive discontinuous Galerkin technique with an orthogonal basis applied to compressible flow problems. *SIAM Review* 2003; **45**(1):53–72.
14. Dennis J, Levy M, Nair R, Tufo H, Voran T. Towards an efficient and scalable discontinuous Galerkin atmospheric model. *IEEE International Parallel and Distributed Processing Symposium*, vol. 14(14), Denver, CO, 2005; 257a.
15. Nair RD, Thomas SJ, Loft RD. A discontinuous Galerkin global shallow water model. *Monthly Weather Review* 2005; **133**(4):876–888.
16. Levy MN, Nair RD, Tufo HM. High-order Galerkin methods for scalable global atmospheric models. *Computers and Geosciences* 2007; **33**(8):1022–1035.
17. Deville MO, Fisher PF, Mund EH. *High-Order Methods for Incompressible Fluid Flow*. Cambridge University Press: Cambridge, 2002.
18. Cockburn B, Shu CW. Runge–Kutta discontinuous Galerkin methods for convection-dominated problems. *Journal of Scientific Computing* 2001; **16**(3):173–261.
19. Nair RD, Thomas SJ, Loft RD. A discontinuous Galerkin transport scheme on the cubed sphere. *Monthly Weather Review* 2005; **133**(4):814–828.
20. Gottlieb S, Shu CW, Tadmore E. Strong stability preserving high-order time integration methods. *SIAM Review* 2001; **43**(1):89–112.
21. Karniadakis GE, Sherwin SJ. *Spectral/hp Element Methods for CFD*. Oxford University Press: New York, NY, 1999.
22. Rančić M, Purser RJ, Mesinger F. A global shallow-water model using an expanded spherical cube: gnomonic versus conformal coordinates. *Quarterly Journal of the Royal Meteorological Society* 1996; **122**(532):959–982.
23. Sadourny R. Conservative finite-difference approximations of the primitive equations on quasi-uniform spherical grids. *Monthly Weather Review* 1972; **100**(2):136–144.
24. Boyd JP. The erfc-log filter and the asymptotics of the Euler and Vandeven sequence accelerations. *Proceedings of the Third International Conference on Spectral and High Order Methods*, Houston, TX, 1996; 267–276.
25. Taylor M, Tribbia J, Iskandarani M. The spectral element method for the shallow water equations on the sphere. *Journal of Computational Physics* 1997; **130**(1):92–108.
26. Chan JCL. The physics of tropical cyclone motion. *Annual Review of Fluid Mechanics* 2005; **37**:99–128.
27. Neamtan SM. The motion of harmonic waves in the atmosphere. *Journal of Meteorology* 1946; **3**(2):53–56.
28. Thuburn J. A PV-based shallow-water model on a hexagonal-icosahedral grid. *Monthly Weather Review* 1997; **125**(9):2328–2347.

DOI: 10.1002/fld